A cascade X-ray energy converting approach toward radio-afterglow cancer theranostics

Cheng Xu[1], Xue Qin[2], Xin Wei[1], Jie Yu[3], Youjia Zhang[4], Yan Zhang[3,*], Dan Ding[5,*], Jibin Song[2,*], Kanyi Pu[1,6,*]

[1] School of Chemistry, Chemical Engineering and Biotechnology, Nanyang Technological University, 70 Nanyang Drive, 637457, Singapore
*E-mail: kypu@ntu.edu.sg
[2] State Key Laboratory of Chemical Resource Engineering, College of Chemistry, Beijing University of Chemical Technology, Beijing 10010, P. R. China
*Email: jibin.song@buct.edu.cn
[3] National Engineering Research Centre for Nanomedicine, College of Life Science and Technology, Hubei Key Laboratory of Bio-inorganic Chemistry and Materia Medical, Huazhong University of Science and Technology1037 Luoyu Road, Wuhan 430074, P.R. China
E-mail: yan_zhang@hust.edu.cn
[4] Department of Nuclear Medicine, China–Japan Union Hospital of Jilin University, Changchun, Jilin, 130033, PR China
[5] Frontiers Science Center for New Organic Matter, Engineering & Smart Sensing Interdisciplinary Science Center, MOE Key Laboratory of Bioactive Materials, and College of Life Sciences, Nankai University, Tianjin 300350, P. R. China
E-mail: dingd@nankai.edu.cn
[6] Lee Kong Chian School of Medicine, Nanyang Technological University, 59 Nanyang Drive, 636921, Singapore

Abstract

Leveraging X-ray to initiate prolonged luminescence (radio-afterglow) and stimulate radiodynamic $^1O_2$ production from optical agents provide opportunities for diagnosis and therapy at tissue depth inaccessible to light. However, X-ray responsive organic luminescent materials are rare due to their intrinsic low X-ray conversion efficiency. Herein, we report a cascade X-ray energy converting approach to develop organic radio-afterglow nanoprobes (RANPs) for cancer theranostics. RANPs comprise a radio wave absorber that down-converts X-ray energy to emit radioluminescence, which is transferred to a radiosensitizer to produce singlet oxygen ($^1O_2$). $^1O_2$ then reacts with a radio-afterglow substrate to generate an active intermediate that simultaneously decomposes to emit radio-afterglow. Through finetuning such a cascade intraparticle radioluminescence energy transfer and $^1O_2$ transfer process, RANPs possess tunable wavelength and long half-life and generate radio-afterglow and $^1O_2$ at a record tissue depth of 15 cm. Moreover, a biomarker-activatable nanoprobe (tRANP) is developed to activate its radio-afterglow signal specific to tumour, leading to an ultrasensitive detection and surgical removal of diminutive tumour (1 mm^3) even under the X-ray dosage 20-times lower than inorganic materials. The efficient radiodynamic $^1O_2$ generation of tRANP permits complete tumour eradication at an X-ray dosage lower than clinical radiotherapy and a drug dosage one to two orders of magnitude lower than most existing inorganic agents, leading to prolonged survival rate with minimized radiation-related adverse effect. Thus, our work reveals a generic approach to fill in the gap of lacking organic radiotheranostic materials and provides molecular design towards precision cancer radiotherapy.

Introduction

Optical imaging allows for the visualization of physio-pathological processes at molecular level, representing an indispensable tool in fundamental research and clinical diagnostics.[1-4] However, the dependence on real-time optical irradiation leads to high autofluorescence and low signal to background ratio (SBR), which compromises the diagnostic sensitivity and specificity.[5] Afterglow imaging leverages the long-lasting light emission after the cessation of irradiation on afterglow agents, minimizing the autofluorescence and leading to a higher SBR and deeper tissue penetration compared to fluorescence imaging.[6,7] Organic afterglow agents store photon energy into chemical defects, which involves photosensitization that generate reactive oxygen species (ROS) and the formation of emissive intermediates to emit afterglow upon decomposition, enabling photodynamic therapy and afterglow imaging for a variety of diseases including cancer, infection, and organ injury.[8-13] However, due to limited light penetration in biological tissues, they are difficult to be induced for theranostics of deep-seated lesions.

Although X-ray is able to penetrate deep tissues, X-ray-induced afterglow (radio-afterglow) materials are limited to few inorganic nanoparticles comprising host matrix (e.g., metal fluorides) and luminescence centre (e.g., rare-earth metal ions).[14] Mechanistically, the host matrix contains high-atomic-number (Z) elements that efficiently harvest X-ray photons by down-converting them to secondary electron-hole pairs. The pairs are trapped in the physical defects of matrix that delay their migration towards luminescence centre, where they recombine to emit radio-afterglow.[15,16] This process could also generate ROS to exert radiodynamic damage on diseased tissues.[17] Since the radiotheranostic functions of inorganic materials are biomarker independent and always active, the diagnostic accuracy and therapeutic efficacies heavily rely on the concentration difference between diseased and normal tissues. By contrast, organic materials have structure versatility for the construction of smart probes with biomarker-activatable radiotheranostic functions;[18,19] however, they often consist of low-Z elements that have inherently low X-ray deposition, which are difficult to induce radio-afterglow and radiodynamic effects. We have recently uncovered that introduction of halogen atoms into certain organic lumiphores can facilitate X-ray absorption and spin-orbit coupling, which led to the only example of radio-afterglow imaging and radiodynamic therapy for organic materials.[20] To fully explore the potential of radio-afterglow cancer theranostics, generic approaches to enhance the conversion of X-ray photon into afterglow luminescence and $^1O_2$ for organic materials are highly desired.

Herein, we report a generic X-ray energy converting approach to develop organic radio-afterglow and radiodynamic nanoagents for cancer theranostics. Radio-afterglow nanoparticle (RANP) comprises a radioabsorber that potently converts X-ray to radioluminescence that transfers to a radiosensitizer, leading to the production of $^1O_2$. $^1O_2$ then can efficiently diffuse to a radio-afterglow substrate to undergo an in-situ reaction to convert it to an active dioxetane intermediate, which simultaneously decomposes and emits long-lasting afterglow after X-ray cessation. Through such as a cascade intraparticle radioluminescence energy transfer (RET) and $^1O_2$ transfer (SOT) process, RANP can be devised to exhibit tuneable near-infrared (NIR) wavelength, long half-life, and superb brightness of radio-afterglow, allowing for the development of smart activatable nanoprobe that only switches on its radio-afterglow in the presence of cancer biomarkers for longitudinal tumour detection and precision tumour surgery in vivo. Moreover, the efficient $^1O_2$ generation enables RANP to exert radiodynamic therapy on cancer at a lower X-ray dosage than clinical radiotherapy, which spares

normal tissues from ionization-associated damage. Thus, RANP represents a generic approach to develop X-ray-based organic theranostic nanoagent with great translational potential.

Composition Screening for RANPs

To optimize radio-afterglow, the composition of RANP was screened. Radioabsorbers were organic agents with high X-ray conversion efficiencies (light yield > 10^4 photons/MeV), including anthracene, polystyrene, 9,10-diphenylanthracene, and 2,4,5,6-tetrakis(3,6-di-tert-butylcarbazol-9-yl)-1,3-dicyanobenzene (CzTPN) (**Fig. 1a and Supplementary Fig. 1**). Radiosensitizers were hematoporphyrin, verteporfin, and silicon 2,3-naphthalocyanine bis(trihexylsilyloxide) (NIR775), due to their bright visible to NIR fluorescence and high $^1O_2$ quantum yields. Radio-afterglow substances were dicyanomethylene-4H-benzothiopyran-phenoxyl-adamantylidene (DPAs) and ((2-(3-((E)-4-hydroxy-2-((1r,5R,7S)-4'-methoxyspiro[adamantane-2,3'-[1,2]dioxetane]-4'-yl)styryl)-5,5-dimethylcyclohexan-1-ylidene)malononitrile) (DTDP), which could form dioxetane intermediate emitting bright near-infrared chemiluminescence.[21,22] The radioabsorber, radiosensitizer and radio-afterglow substate were co-loaded into nanoparticles using amphiphilic polymers as the matrix via nanoprecipitation method, including poly(ethylene glycol)-block-poly(propylene glycol)-block-poly (PEG-PPG-PEG, Pluronic F127), poly(lactic-co-glycolic acid) (PLGA)-PEG, or 2-distearoyl-sn-glycero-3-phosphoethanolamine-PEG (DSPE-PEG).

CzTPN-loaded nanoparticles emitted brighter afterglow than those loaded with other radioabsorbers, which could be mainly attributed to its highest light yield (4.5×10^4 photons/MeV) (**Fig. 1b, c**). Moreover, hematoporphyrin-loaded nanoparticles exhibited higher radio-afterglow signals than verteporfin- and NIR775-loaded nanoparticles, in line with their $^1O_2$ generation yields. Furthermore, DTDP-loaded nanoparticles emitted brighter radio-afterglow than DPAs-loaded nanoparticles, probably because of its higher chemiluminescence quantum yield was ~20 times higher than that of DPAs. Nevertheless, DTDP had a short emission wavelength (peak at 552 nm) that could be attenuated in biological tissues, restraining their deep tissue imaging in vivo (**Supplementary Fig. 2 and 3**). Thus, NIR775 with absorption spectral overlap (with DTDP emission) and fluorescence peaked at 788 nm was chosen as radiosensitizers to 'relay' energy from DTDP, despite its moderate $^1O_2$ generation ability. In addition, F127 nanoparticles emit brighter radio-afterglow than in DSPE-PEG and PLGA-PEG nanoparticles under same mass concentration (**Fig. 1d and Supplementary Fig. 4**). This could be attributed to the most compact size of F127 nanoparticles that led the shortest X-ray energy transfer distances among three nanoparticles. Collectively, RANP comprising CzTPN as radioabsorber, NIR775 as radiosensitizer, DTDP as radio-afterglow substrate, and F127 as vehicle was chosen for subsequent mechanistic experiments.

Cascade X-ray energy converting mechanism

To study the mechanism of radioafteglow, radioluminescence (light emission under real-time X-ray irradiation) was first tested in F127 nanoparticles loading CzTPN alone (**Fig. 2a, b**). Under X-ray irradiation, CzTPN nanoparticles emitted bright radioluminescence with the emission maximum at 563 nm, similar to the fluorescence spectrum upon excitation at the maximum absorption of CzTPN at 420 nm (**Supplementary Fig. 5**). This suggested that radioluminescence from CzTPN involved '$S_1 \rightarrow S_0$' relaxation. Moreover, the radioluminescence intensities were increased with escalating tube current of X-ray (0-0.5 mA) and CzTPN amount in nanoparticles (**Supplementary Fig. 6, 7**). The highest signal was measured at a mass ratio of CzTPN to F127 at 1:50; precipitation was observed

beyond that ratio. At this mass ratio, anthracene or polystyrene loaded F127 showed the radioluminescence signals 4 and 10 times lower than CzTPN nanoparticles (**Supplementary Fig. 8**), respectively. The relatively higher radioluminescence brightness of CzTPN nanoparticles relative to others coincided with its high light yield of CzTPN, which should be mainly attributed to its low energy gap between S_1 and T_1 (ΔE_{ST} < 0.1 eV) that facilitates reverse intersystem crossing and electron-rich donor-acceptor structure that improves intramolecular electron transfer.[23-25]

To test the X-ray energy transfer from radioabsorber to radiosensitizer and radiodynamic effect, NIR775 was loaded alone or co-loaded with CzTPN into F127 nanoparticles. Negligible radioluminescence was detected from NIR775 nanoparticles above 750 nm; by contrast, brighter signals were shown in CzTPN/NIR775 nanoparticles and were 30 times brighter than that in CzTPN nanoparticles (**Fig. 2b**). Moreover, the radioluminescence spectrum of CzTPN/NIR775 nanoparticles resembled the fluorescence spectrum excited at 420 nm (**Fig. 2c**), showing two characteristic peaks corresponding to CzTPN at 563 nm and NIR775 at 788 nm (**Supplementary Fig. 5**). With increased doping amount of NIR775, NIR radioluminescence increased at the expense of the visible radioluminescence from CzTPN, showing the highest intensity at a mass ratio of 1: 10 (molar ratio of 1: 10.8, NIR775 to CzTPN) with the RET efficiency of 68.9% (**Fig. 2d**). The sharp decrease of NIR radioluminescence beyond that ratio should be caused by the self-quenching of NIR775. Apart from radioluminescence, NIR775/CzTPN nanoparticles generated $^1O_2$ that were 100 and 156 times higher than mono- NIR775 or CzTPN nanoparticles under equivalent mass concentrations (**Fig. 2e**). The highest $^1O_2$ generation yield was generated at a doping ratio of 1: 10 (NIR775 to CzTPN, w/w), in line with the optimal ratio for radioluminescence (**Fig. 2f**). Moreover, $^1O_2$ generation increased with X-ray dosages and concentrations of CzTPN/NIR775 nanoparticles (**Supplementary Fig. 9**). However, no superoxide anion or hydroxyl radicals was detected (**Supplementary Fig. 10**), indicating that $^1O_2$ was produced from NIR775, a typical type-II photosensitizer. Collectively, these data validated the RET process from CzTPN to NIR775, leading to NIR radioluminescence (via '$S_1 \rightarrow S_0$' relaxation) and $^1O_2$ production (via '$T_1 \rightarrow S_0$' relaxation) (**Fig. 2g**).

After confirming the occurrence of RET and radiodynamic $^1O_2$ generation, DTDP was co-loaded with CzTPN and NIR775 to study the radio-afterglow mechanism (**Fig. 3a**). After cessation of X-ray irradiation, bright radio-afterglow was observed only for RANP rather than mono-system (e.g., DTDP nanoparticles) or binary system (e.g., CzTPN/DTDP nanoparticles), indicating that each component was indispensable for radio-afterglow (**Fig. 3b, c)**. Moreover, the radio-afterglow spectrum of RANP peaked at 552 and 788 nm corresponding to DTDP and NIR775, respectively, which resembled its fluorescence spectrum upon excitation of DTDP at 430 nm. The presence of DTDP afterglow emission confirmed the formation of chemiluminescent DTDP intermediate induced by cycloaddition reaction with $^1O_2$ generated by NIR775; whereas the NIR775 afterglow emission proved the partial chemiluminescent energy transfer from the intermediate DTDP to NIR775, allowing RANP to achieve a record long radio-afterglow at 788 nm for existing organic materials (**Fig. 3d and Supplementary Fig. 11**). The radio-afterglow intensities of RANP increased with escalating X-ray dosage with a limit of detection of 0.046 mGy, showing its high X-ray responsiveness (**Supplementary Fig. 12**). It also exhibited a half-life of 4.8 min and a lifetime over 12 h, and its intensities maintained after five cycles of X-ray irradiation, indicating the rechargeability (**Fig. 3e and Supplementary Fig. 13**).

Based on these observations, the radio-afterglow mechanism via a cascade X-ray energy converting

approach was proposed (**Fig. 3g**). Owing to the high light yield, radioabsorbers attenuate X-ray via photoelectric and Compton effects, resulting in scintillation and radioluminescence. The radioluminescence can then be transferred to radiosensitizers (RET process) to generate $^1O_2$. $^1O_2$ is subsequently transferred to radio-afterglow substrates (SOT process), oxidizing them to self-luminescent intermediates of high chemical energy. These intermediates gradually decompose to emit the long-last luminescence (radio-afterglow). The yielded radio-afterglow could also be able to transfer back to radiosensitizer, causing the red-shifted radio-afterglow from radiosensitizers. With an optimal hydrodynamic diameter of 94.2 ± 2.6 nm, a slightly negative surface charge of -6.3 ± 1.1 mV, and a spherical shape (transmission electron microscopy) (**Fig. 3f and Supplementary Fig. 14, 15**), RANP comprising CzTPN as radioabsorber, NIR775 as radiosensitizer, DTDP as radio-afterglow substrate, and F127 as vehicle should have ideal blood circulation and tumour accumulation.

In vitro studies of radio-afterglow imaging depth and radiodynamic cytotoxicity

To demonstrate deep-tissue radio-afterglow, RANP was irradiated by X-ray or laser with chicken breast tissues of different thicknesses (**Fig. 4a**) and then the signal was detected after removing chicken breast tissues. Note that X-ray and laser irradiation conditions were adjusted to afford the same afterglow intensities without chicken breast coverage (**Fig. 4b, c**). Both photoafterglow and radio-afterglow intensities decreased with the increased tissue thickness, while radio-afterglow was brighter than photoafterglow at all depths, showing 50 times higher in signals at the tissue depth of 2.5 cm. Radio-afterglow was still detectable at 15 cm (SBR 3.7), while photoafterglow was hardly detectable at 5 cm (SBR 2.3). Moreover, when both pre-irradiation and signal acquisition were conducted through tissues, radio-afterglow was detectable at 5 cm (SBR 5.9), in sharp contrast to that of 1.5 cm by photoafterglow (SBR 5.0) (**Supplementary Fig. 16**). To gain insight into the brighter radio-afterglow in deep tissue relative to photoafterglow, $^1O_2$ generation from RANP under X-ray or laser irradiation was studied (**Fig. 4d**). Without tissue coverage, X-ray and laser irradiation conditions were controlled to make $^1O_2$ generated by RANP the same. the maximum depth to induce $^1O_2$ generation was 15 and 5 cm for X-ray and laser irradiations, respectively. These data confirm that the superior deep-tissue imaging of radio-afterglow as compared to photoafterglow is due to the higher $^1O_2$ yield of the radiodynamic process relative to the photodynamic process in deep tissues.

The radio-afterglow imaging and radiodynamic effect of RANP was studied in 4T1 and MCF-7 cancer cells. After incubation with RANP for 12 h, radio-afterglow signal from cells was observed, verifying the cellular uptake of RANP (**Fig. 4e, f**). In contrast, radio-afterglow signal was negligible for cells treated with single-component nanoparticles (i.e., CzTPN nanoparticles, NIR775 nanoparticles, and DTDP nanoparticles) (**Supplementary Fig. 17, 18**). The radiodynamic cytotoxicity of RANP was studied at various incubation concentrations (5-80 μg/mL) by cell counting kit-8 assay (CCK-8) (**Fig. 4g**). Without X-ray irradiation, cells showed negligible death even at the highest RANP concentration; by contrast, the cell viability decreased with increasing dose of X-ray from 0.01 Gy to 2 Gy (**Supplementary Fig. 19**), showing only 10% at 0.5 Gy. Even through 15 cm-thick tissue, 70% of cells killing could be achieved, verifying the feasibility of RANP-mediated radiodynamic therapy in deep tissue (**Supplementary Fig. 20**). Cells after treatment were further stained with fluorescein isothiocyanate (FITC)-tagged annexin and propidium iodide (PI), followed by analysis with flow cytometry (**Supplementary Fig. 21**). RANP-treated and X-ray-irradiated cells showed the least population of living cells (approximately 20%), consistent with cytotoxicity assay. Note that early apoptotic cells (annexin-FITC^{high}/PI^{low}) accounted for approximately 52% of cells, ~ 5 times higher

than other groups. This suggested that apoptosis should be a major way of cell death by RANP-mediated radiodynamic therapy, which potentially enhanced immunogenicity to benefit tumour immunotherapy.

To verify the radiodynamic cytotoxic mechanism, cells after different treatments were pre-incubated with dichloro-dihydro-fluorescein diacetate (DCFH-DA), a turn-on fluorescent sensor for intracellular ROS detection. The CLSM (confocal laser scanning microscope) images (**Fig. 4h, i**) showed that the fluorescence of RANP-treated X-ray-irradiated cells was >9.5 times higher than that of other groups. Moreover, if the cells were pretreated with tryptophan ($^1O_2$ scavenger) prior to RANP incubation, the cellular viability increased by 4-fold as compared to that without tryptophan treatment (**Supplementary Fig. 22**). Cells treated with NIR775-free RANP showed increased viability compared to those treated with RANP. Similar tumor killing effect of RANP was observed for MCF-7 cells (**Supplementary Fig. 23-25**).

In vivo radio-afterglow cancer theranostics

To enable precision radio-afterglow imaging, tumour-specific RANP (tRANP) was developed to activate its radio-afterglow only in the presence of H_2O_2, which was upregulated in tumour (**Fig. 5a and Supplementary fig. 26**).[26] DTDP was caged by phenylborate ester (a moiety specifically oxidized by H_2O_2) (ref. [27]), affording cDTDP with diminished intramolecular charge transfer and thus inhibited afterglow emission (**Supplementary scheme. 1**). In the presence of H_2O_2, the caging group of cDTDP in tRANP was cleaved, as verified by a new elution peak at 17 min in the high-performance liquid chromatography (HPLC), leading to a 40-fold increase of radio-afterglow (**Fig. 5b and Supplementary Fig. 27**). Moreover, the radio-afterglow spectral profile of H_2O_2-treated tRANP resembled its fluorescence (**Supplementary Fig. 28**). tRANP had a superb selectivity towards H_2O_2 over other reactive species such as superoxide anion ($O_2^{\cdot-}$), nitric oxide (NO), and hydroxyl radicals (·OH) (**Supplementary Fig. 29**). The biomarker-activatable radio-afterglow was observed in 4T1 cells treated with H_2O_2 and X-ray irradiation, showing 8- and 11-times higher signal than those with X-ray or H_2O_2 treatment alone (**Supplementary Fig. 30**).

To study tumour-specific radio-afterglow in vivo, tRANP was subcutaneously injected to the left flank and intratumorally injected to 4T1 tumour on the right flank of mice, respectively (**Fig. 5c**). At 10 min post-injection, the injection sites were irradiated with X-ray prior to radio-afterglow acquisition. The radio-afterglow signal on tumours was 39 times higher than that on subcutaneous sites, with an SBR as high as 169 vs 14 for fluorescence signals (**Fig. 5d, e**). Next, tRANP was intravenously injected to tumour-bearing mice, and its biodistribution was longitudinally monitored (**Fig. 5f**). Both fluorescence and radio-afterglow signals on tumours increased over time and peaked at 24 h. At this timepoint, the SBR of radio-afterglow (207) was 18 times higher than fluorescence (11), showing the superiority of radio-afterglow over fluorescence in in vivo cancer detection (**Fig. 5g, h**). Such a high SBR for subcutaneous tumor detection was one order of magnitude higher than most existing inorganic materials (for example, 16.5 for $ZnGa_2O_4:Cr^{3+}$) and comparable to the only reported organic probe (for example, 234 for MRAP) (**Supplementary Table 1**).[20,28] Moreover, due to the high responsiveness to ionization, tRANP could be recharged with a minimal X-ray dose of 1 mGy after a single injection, and such dose was at least 20- and 5-times lower than the inorganic materials and the organic probe, respectively.[20] Ex vivo imaging showed that tRANP was mostly accumulated in tumour (owing to the optimal size and surface charge), followed by liver and spleen (**Supplementary**

Fig. 31).

The capability of imaging-guided surgery was tested in a peritoneal metastasis model established by intraperitoneal inoculation of 4T1 cells into mice (**Fig. 5i**). At 7 days post-inoculation, mice were intravenously injected with tRANP for radio-afterglow imaging. Tumours were clearly delineated by radio-afterglow signals in both intact (SBR = 53) and abdomen-open mice (SBR = 122); by contrast, they were indistinguishable from surrounding tissues by fluorescence imaging due to its high background noises (**Fig. 5j, k**). The stark contrast provided by radio-afterglow imaging enabled a complete resection of diminutive tumours as small as 1 mm^3, which were confirmed by histological analysis (**Supplementary Fig. 32**).

To study the in vivo radiodynamic therapeutic efficacy, subcutaneous 4T1 tumour-bearing mice were intravenously injected with tRANP, and tumours were irradiated with 3 fractions of X-ray (1 Gy per fraction), which was optimized in pilot assays (**Fig. 6a and Supplementary Fig. 33**). Mice with X-ray irradiation or tRANP alone were set for comparison. tRANP plus X-ray irradiation completely suppressed tumour growth with the tumour inhibition rate as high as 97.2%, and no recurrence even after three weeks post-treatment; by contrast, tRANP alone had negligible tumour inhibition, showing the growth curve similar with PBS-treated group (**Fig. 6b**). X-ray irradiation alone had a slight inhibitory effect, and tumours were reinvigorated on day 11. The efficient tumour eradication by tRANP coupled with low-dose X-ray contributed to the prolonged survival of tumour-bearing mice up to one-month post-treatment (**Fig. 6c**). Note that the complete tumour eradication could also be achieved by X-ray irradiation alone at a dosage 6 times higher than tRANP-mediated radiodynamic therapy, which was equivalent to the X-ray dosage for clinical radiotherapy (3 fractions of X-ray, 6 Gy per fraction) (**Supplementary Fig. 34**).[29,30]

The mechanism for effective tumour inhibition of tRANP was further analysed by injecting $^1O_2$ sensor green (SOSG) into tumours of mice after indicated treatments. Following X-ray irradiation (1 Gy), tumours were collected and sliced for fluorescence imaging. tRANP plus X-ray elicited the highest fluorescence of SOSG in tumours among all groups (**Fig. 6d, e**), confirming the efficient intra-tumoral generation of $^1O_2$. As a result, tRANP-mediated radiodynamic therapy led to the largest area of tumour damage among groups, as characterized by vanished nuclei and broken cell morphology, as well as the highest expression level of caspase-3 (apoptotic biomarker) (**Fig. 6f to i**); besides, it elicited the highest expression levels of calreticulin (CRT) and high mobility group box 1 (HMGB-1), suggesting the occurrence of immunogenic cell death (**Supplementary Fig. 35**). Consequently, mice after tRANP-mediated radiodynamic therapy possessed the least metastatic nodules in lung (**Fig. 6j, k**).

Radiodermatitis is a common radiation-associated adverse effect characterized by skin peeling, lupus, and edema.[31] Mice receiving traditional radiotherapy (6 Gy × 3 fractions) showed skin damage and immune cell infiltration in the tumour-adjacent skin at 7 days post treatment despite its ability to inhibit the tumour growth; by contrast, tumour-adjacent tissue of mice treated with tRANP-mediated radiodynamic therapy was spared from damage (**Supplementary Fig. 36**). This was attributed to the lower doses for tRANP-based therapy, which was also lower than that of most existing radiosensitizers in preclinical tumour radiodynamic therapy (**Supplementary Table 2**). No measurable body weight loss nor histological abnormality was observed (**Supplementary Fig. 37,**

38). Additionally, the indicators for blood biochemistry and hepatic/renal functions were within normal ranges, showing the safety of tRANP-mediated radiodynamic therapy (**Supplementary Fig. 39 and Supplementary Table 3**).

Conclusion

This study reports a generic and efficient approach via X-ray energy and singlet oxygen cascade transfer process to construct the first example of organic radio-afterglow and radiodynamic nanoparticles (RANPs) and reveals the key parameters governing the radiotheranostic efficacies. The modular composition and well-defined mechanism of RANPs enabled finetuning their radio-afterglow wavelength, brightness, and biomarker responsiveness, leading to a smart cancer-specific radiotheranostic nanoprobe. RANP has the potential not only for ultrasensitive detection of diminutive lesions at excipient stage but also for precise and safe radiotherapy of deep-seated diseases beyond cancer at a minimal dosage. Moreover, the similarity in X-ray settings between a CT scanner and RANP makes it feasible to further develop bimodal imaging probes. This advancement would allow for the simultaneous acquisition of both anatomical and molecular information of diseases in a single CT scan. RANP was only tested in tumor models in this work, and more disease models in a wider range of organisms could be validated in the future. Collectively, our work reveals a generic approach to fill in the gap of lacking organic radiotheranostic biomaterials and provides molecular design towards precision radiotherapy.

Acknowledgements

Y.Z. thanks National Natural Science Foundation of China (22322406) for financial support. D.D. thanks the National Natural Science Foundation of China (52225310) for financial support. J.S. thanks the National Natural Science Foundation of China (No. 21874024, U21A20377, U22A20348), Fundamental Research Funds for the Central Universities (buctrc202235), and the National Key Research and Development Plan (NO. 2023YFB3810002). K.P. thanks the Singapore National Research Foundation (NRF) (NRF-NRFI07-2021-0005) and the Singapore Ministry of Education Academic Research Fund Tier2 (MOE-T2EP30220-0010 and MOE-T2EP30221-0004) for financial support. We thank Du Shiye from China–Japan Union Hospital of Jilin University, and Li Qingqing and Liu Xing from Beijing University of Chemical Technology for the assistance in the equipment operation.

Author contributions

K.P. conceived the study. K.P. Y. Z., and C.X. designed the experiments. C.X. and X.Q. prepared nanomaterials and conducted in vitro characterization. X.W. conducted chemical synthesis. C.X. J. Y., and Y. Z. conducted cell experiments. C.X. performed in vivo experiments. K.P., J. S., Y. Z. D.D., and C.X. analysed the data and drafted the manuscript.

Competing interests

The authors declare no conflict of interest.

Figures

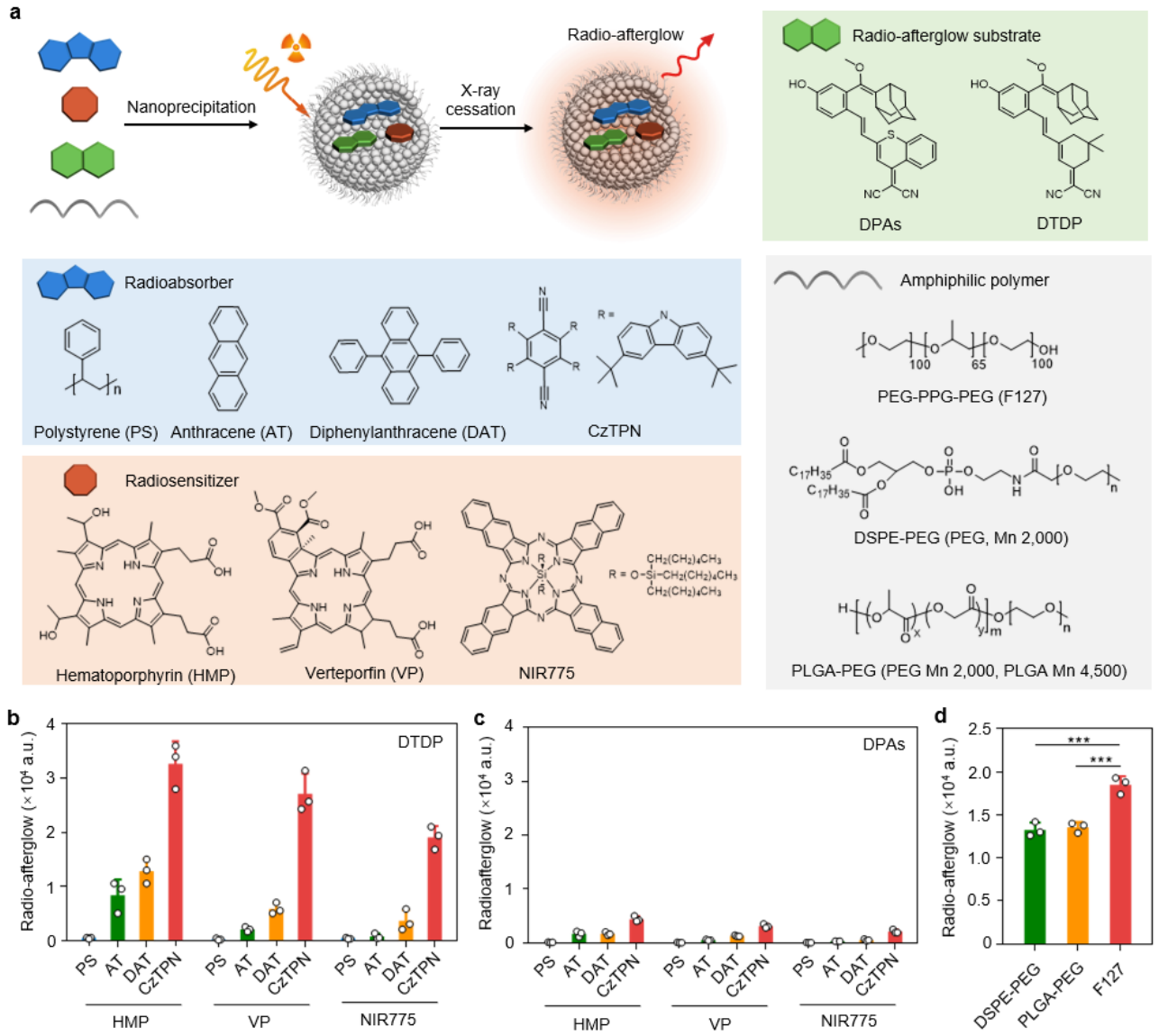

Fig. 1 | Screening of radio-afterglow composition. (a) Radio-afterglow induction from amphiphilic nanoparticles containing a variety of radioabsorbers, radiosensitizers, radio-afterglow substrates and amphiphilic polymers. **(b, c)** Radio-afterglow intensities of DTDP-based nanoparticles (b) and DPAs-based nanoparticles (c) with different radioabsorbers and radiosensitizers. [Radioabsorber] = 100 μg/mL, [Radiosensitizer] = 10 μg/mL, [Radio-afterglow substrate] = 25 μg/mL. F127 as the amphiphilic polymer for all RANPs. **(d)** Radio-afterglow intensities of nanoparticles assembled by different amphiphilic polymers. [CzTPN] = 100 μg/mL, [NIR775] = 10 μg/mL, [DTDP] = 25 μg/mL. ***p = 0.000559 (DSPE-PEG), *** p = 0.000772. For all experiments, n = 3 independent samples. Data were presented as mean ± s.d. Statistical significance was calculated via one-way ANOVA followed by Tukey's post hoc test in (d).

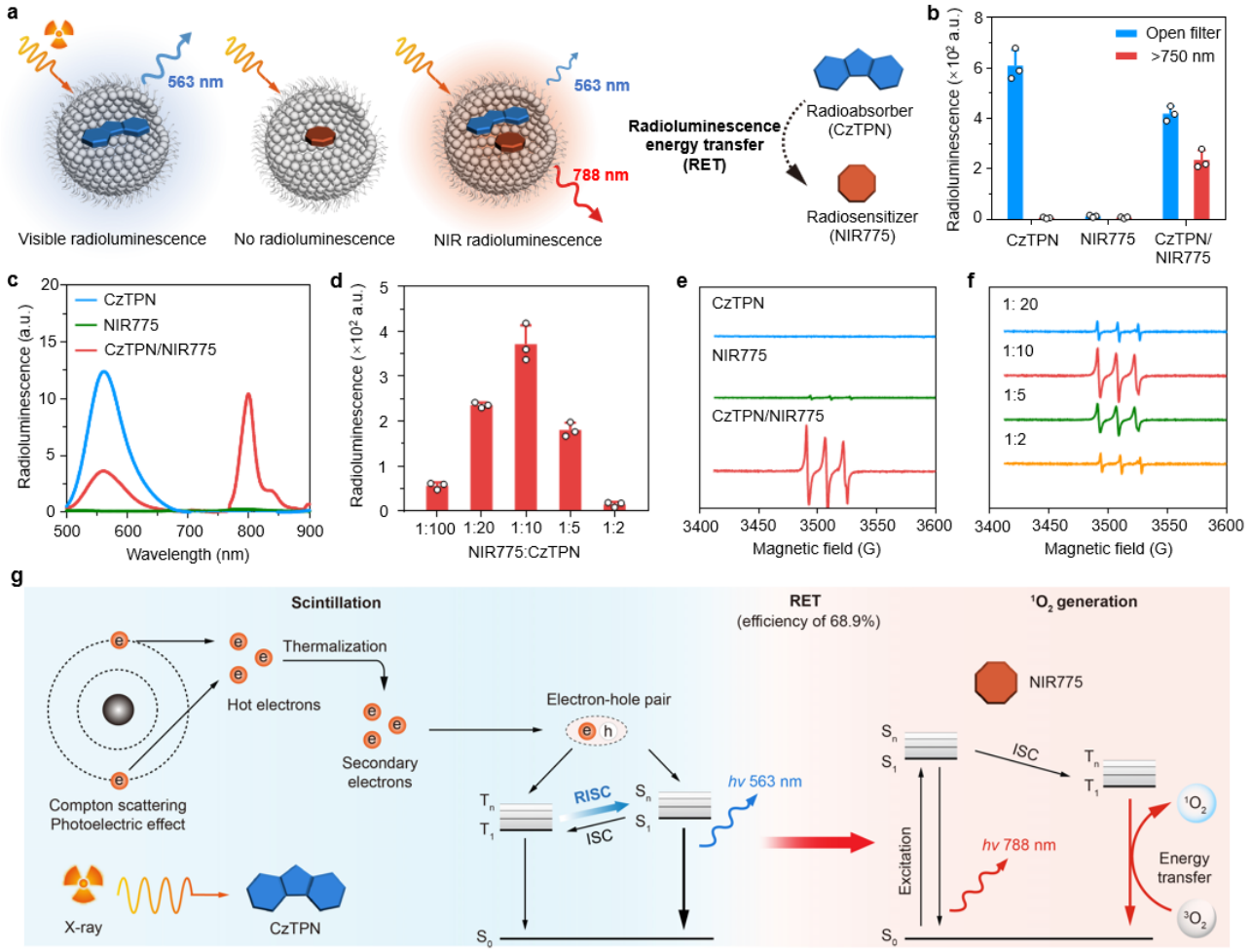

Fig. 2 | Radioluminescence energy transfer (RET). (a) Schematic of RET within nanoparticles comprising CzTPN (radioabsorber) and NIR775 (radiosensitizer). **(b)** Radioluminescence of CzTPN, NIR775 and CzTPN/NIR775 nanoparticles under real-time X-ray irradiation (50 kV, 200 μA). [CzTPN] = 100 μg/mL, [NIR775] = 10 μg/mL, n = 3 independent samples. **(c)** Radioluminescence spectra of CzTPN, NIR775 and CzTPN/NIR775 nanoparticles in 0.01 M phosphate buffered saline (PBS). [CzTPN] = 100 μg/mL. **(d)** NIR radioluminescence intensities of CzTPN/NIR775 nanoparticles (in 0.01 M PBS) at different mass doping ratios under real-time X-ray irradiation (50 kV, 200 μA). [CzTPN] = 100 μg/mL, n = 3 independent samples. **(e)** ESR spectra of $^1O_2$ generation from CzTPN, NIR775 and CzTPN/NIR775 nanoparticles. [CzTPN] = 100 μg/mL, [NIR775] = 10 μg/mL. **(f)** ESR spectra of $^1O_2$ generation from CzTPN/NIR775 nanoparticles at different mass doping ratios. [NIR775] = 10 μg/mL for all groups. **(g)** Proposed mechanism of RET in RANP. Radioabsorber (CzTPN) down-coverts X-ray to radioluminescence via photoelectric effect and Compton scattering (scintillation). The radioluminescence is transferred to radiosensitizer (NIR775) to emit NIR radioluminescence and generate $^1O_2$. ISC, intersystem crossing. RISC, revserse intersystem crossing. Data were presented as mean ± s.d.

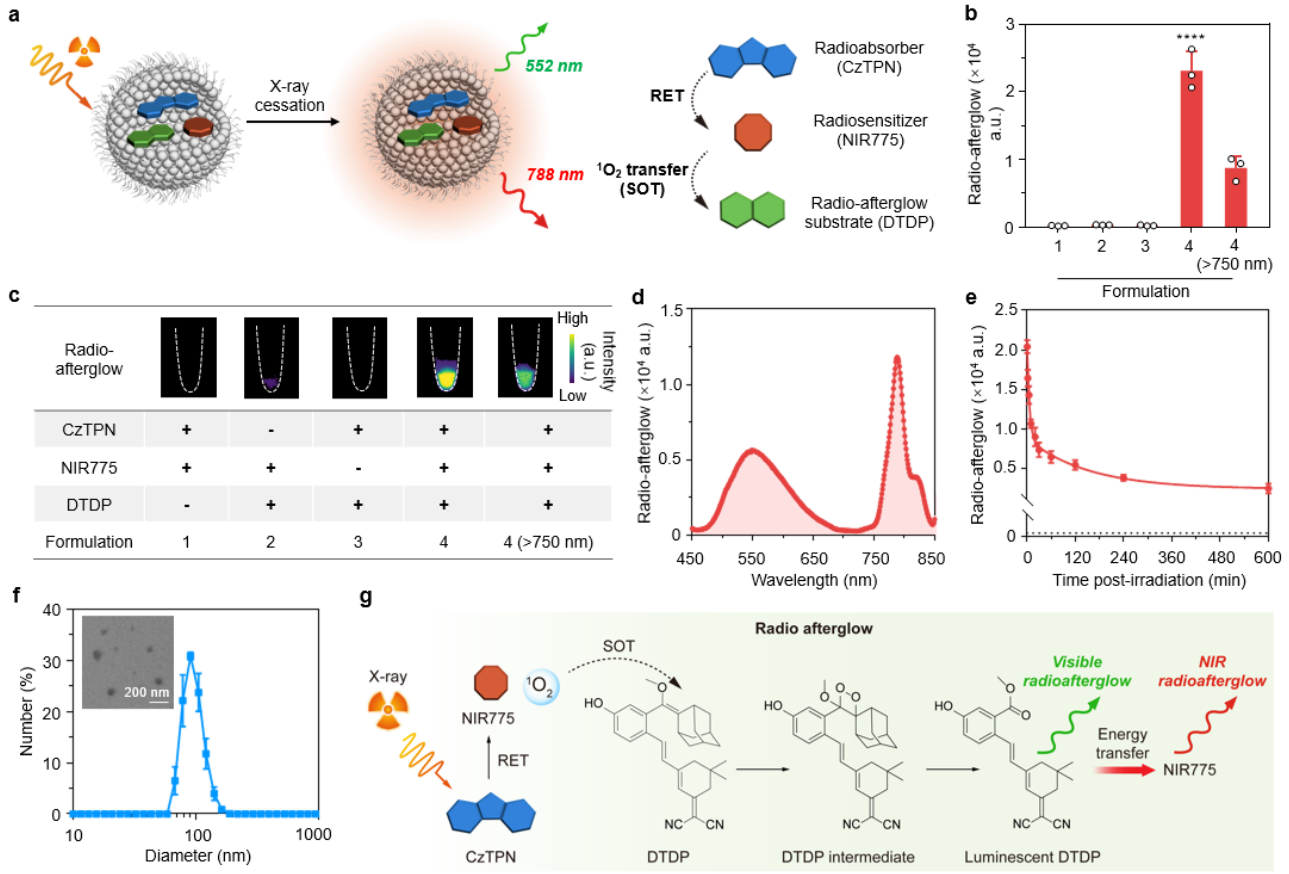

Fig. 3 | Radio-afterglow Mechanism. (a) Radio-afterglow from RANP comprising radioabsorber (CzTPN), radiosensitizer (NIR775), and radio-afterglow substrate (DTDP) via cascade intraparticle RET and SOT. **(b, c)** Quantification (b) and radio-afterglow images (c) of nanoparticles with different formulations in PBS (0.01 M, pH7.4). [CzTPN] = 100 μg/mL, [NIR775] = 10 μg/mL, [DTDP] = 25 μg/mL. 750 LP, 750 nm long pass filter. X-ray dosage, 1 mGy. n = 3 independent samples. **** $p <$ 0.0001 versus formulation 1 (2.5×10^{-7}), formulation 2 (2.6×10^{-7}) and formulation 3 (2.5×10^{-7}). **(d)** Radio-afterglow spectrum of RANP in PBS (0.01 M pH 7.4) after X-ray pre-irradiation (1 mGy). [DTDP] = 25 μg/mL. **(e)** Radio-afterglow decay of RANP in PBS after X-ray pre-irradiation (1 mGy). [DTDP] = 25 μg/mL. Dashed line indicated background level. n = 3 independent samples. **(f)** Size and representative TEM image (inset) of RANP. [DTDP] = 10 μg/mL. n = 3 independent samples. **(g)** Proposed mechanism of radio-afterglow in RANP. Data were presented as mean ± s.d. Statistical significance was calculated via one-way ANOVA followed by Tukey's post hoc test (b).

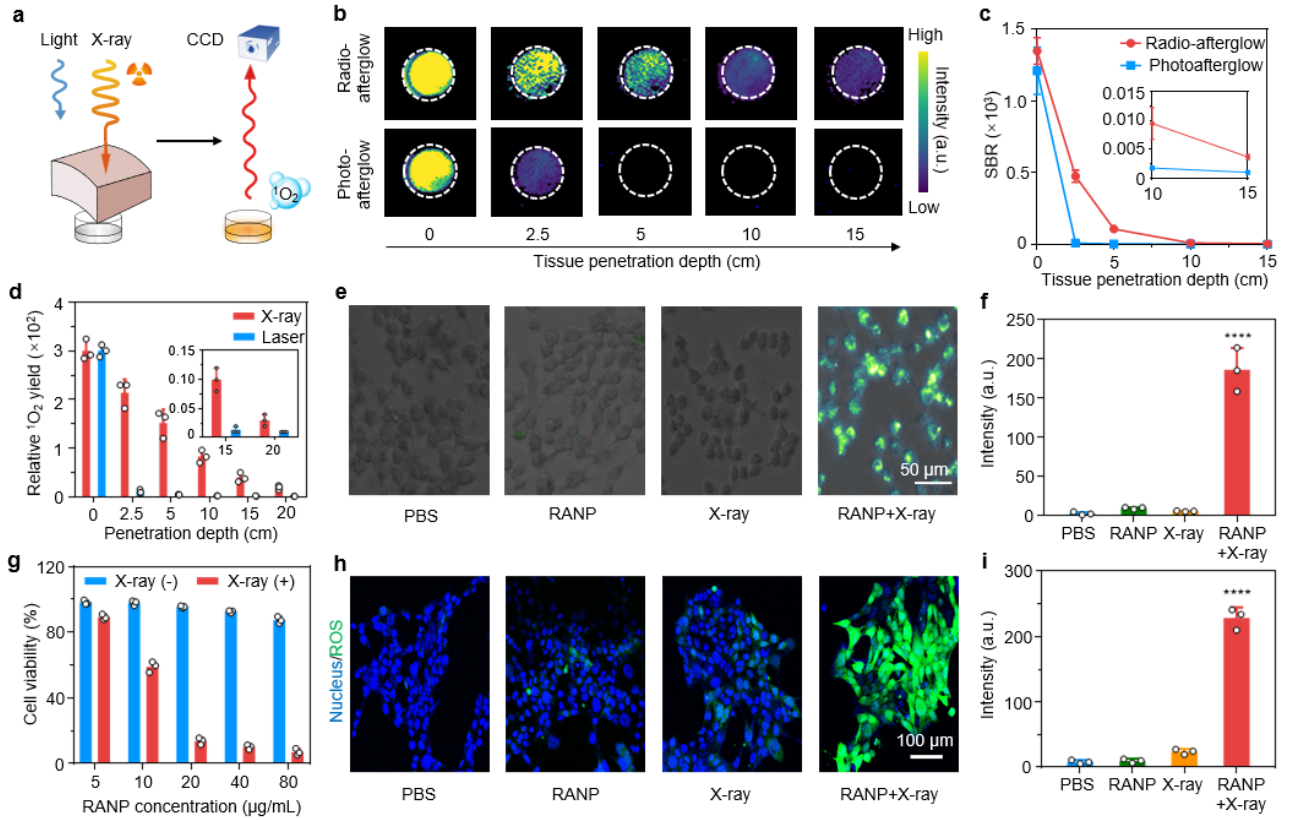

Fig. 4 | In vitro studies of radio-afterglow imaging depth and radiodynamic cytotoxicity. (a) Schematic showing the induction and detection of radio-afterglow or photoafterglow through chicken breast tissue. CCD, charge-coupled device. **(b, c)** Representative images (b) and SBRs (c) for radio-afterglow and photoafterglow of RANP ([DTDP] = 100 μg/mL) induced by X-ray (50 kV, 200 μA) or laser (680 nm) through chicken breast tissue of different thicknesses (n = 3 independent samples). **(d)** Relative $^1O_2$ generation from RANP ([NIR775] = 40 μg/mL) induced by X-ray (50 kV, 200 μA) or laser (680 nm) through chicken breast tissues of different thicknesses (n = 3 independent samples). **(e)** Radio-afterglow images of 4T1 cancer cells after indicated treatments. X-ray dosage, 1 mGy. RANP, [DTDP] = 20 μg/mL. Images were captured by microscope without any excitation. Acquisition time: 10 s. **(f)** Quantification of radio-afterglow intensities in (e) (n = 3 independent samples). **** $p < 0.0001$ versus PBS (1×10^{-5}), RANP (1×10^{-5}) and X-ray (1×10^{-5}). **(g)** Cell viability of 4T1 cancer cells incubated with RANP at different concentrations (equivalent to NIR775) and irradiated with or without X-ray (0.5 Gy) (n = 3 independent samples). **(h)** Confocal microscopic images of 4T1 cancer cells stained with dichloro-dihydro-fluorescein diacetate (DCFH-DA, green) after indicated treatments. Cells were incubated with or without RANP ([NIR775] = 20 μg/mL) for 12 h, followed by irradiation with or without X-ray (0.5 Gy). **(i)** Quantification of DCFH-DA fluorescence intensities in (h) (n = 3 independent samples). **** $p<0.0001$ versus PBS (5.8×10^{-9}), RANP (6.1×10^{-9}) and X-ray (1×10^{-8}). Data were presented as mean ± s.d. Statistical significance was calculated via one-way ANOVA followed by Tukey's post hoc test (f and i).

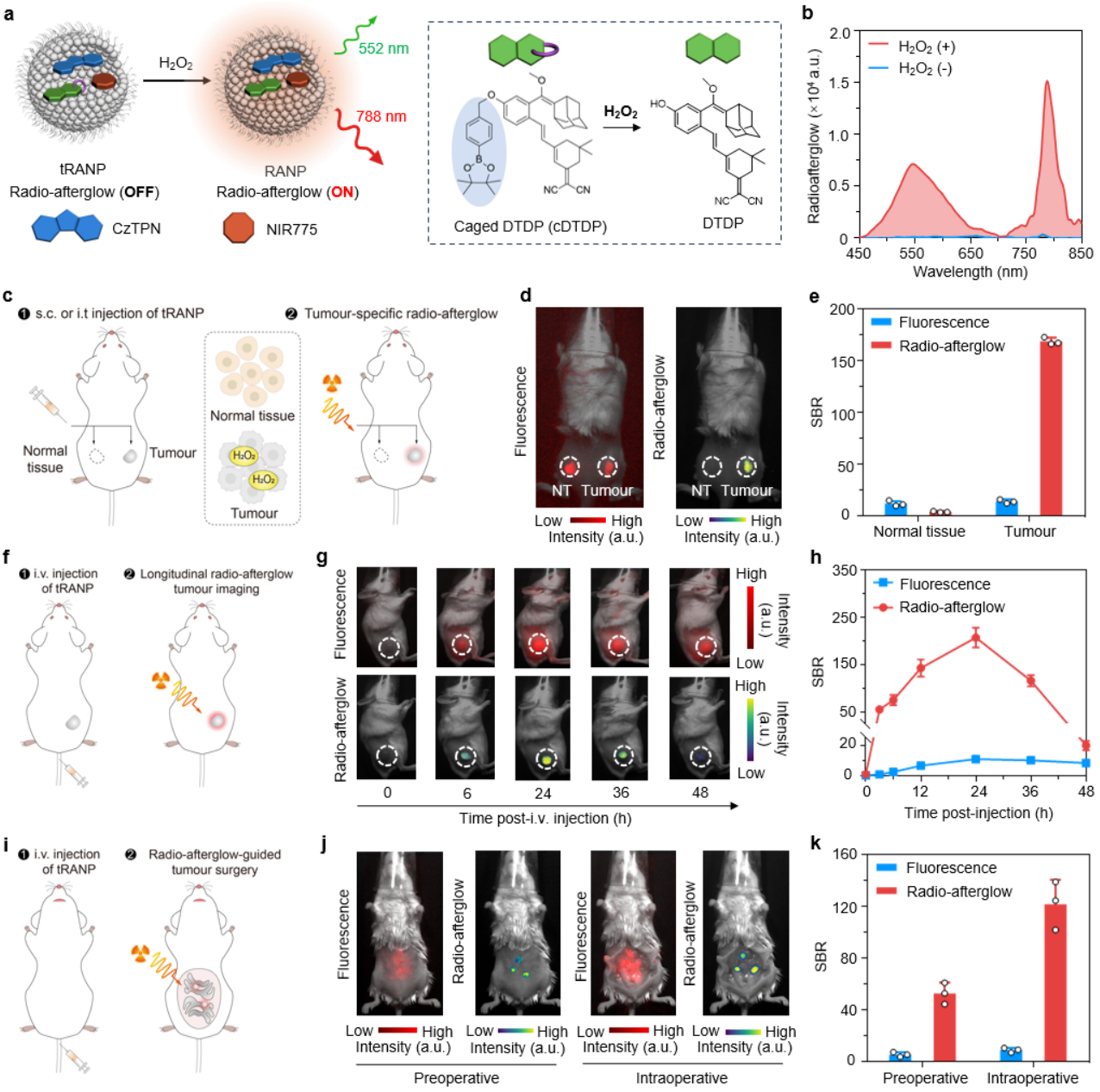

Fig. 5 | Tumour-specific in vivo radio-afterglow imaging. (a) Molecular mechanism of tRANP for activatable radio-afterglow imaging of cancer. H_2O_2 overproduced in tumour microenvironment cleaves the phenylboronic ester of caged DTDP (cDTDP), turning on radio-afterglow. **(b)** Radio-afterglow spectra of tRANP ([DTDP] = 10 μM) treated with or without H_2O_2 (20 μM). **(c)** Schematic of tumour-specific radio-afterglow. tRNAP was subcutaneously and intratumorally injected onto mice, followed by X-ray irradiation at both sides for radio-afterglow imaging. **(d)** Representative fluorescence and radio-afterglow images of mice locally injected with 10 μL of tRANP ([cDTDP] = 100 μg/mL). NT, normal tissue. **(e)** SBRs of fluorescence and radio-afterglow signals on injection sites in (d) (n = 3 mice). **(f)** Schematic of longitudinal imaging of tumour. tRNAP was intravenously injected to subcutaneous 4T1 tumour mice, followed by X-ray pre-irradiation for radio-afterglow imaging. **(g)** Representative fluorescence and radio-afterglow images of mice intravenously injected with 100 μL of tRANP ([cDTDP] = 250 μg/mL). **(h)** SBRs of fluorescence and radio-afterglow on tumours in (g) (n = 3 mice). **(i)** Schematic of radio-afterglow-guided laparotomy of peritoneal metastatic tumours. **(j)** Representative pre-operative and intraoperative images of peritoneal tumour-

bearing mice intravenously injected with 100 μL of tRANP ([cDTDP] = 250 μg/mL) under fluorescence and radio-afterglow imaging. **(k)** SBRs of fluorescence and radio-afterglow on metastatic tumours of mice during laparotomy in (j) (n = 3 mice). Data were presented as mean ± s.d.

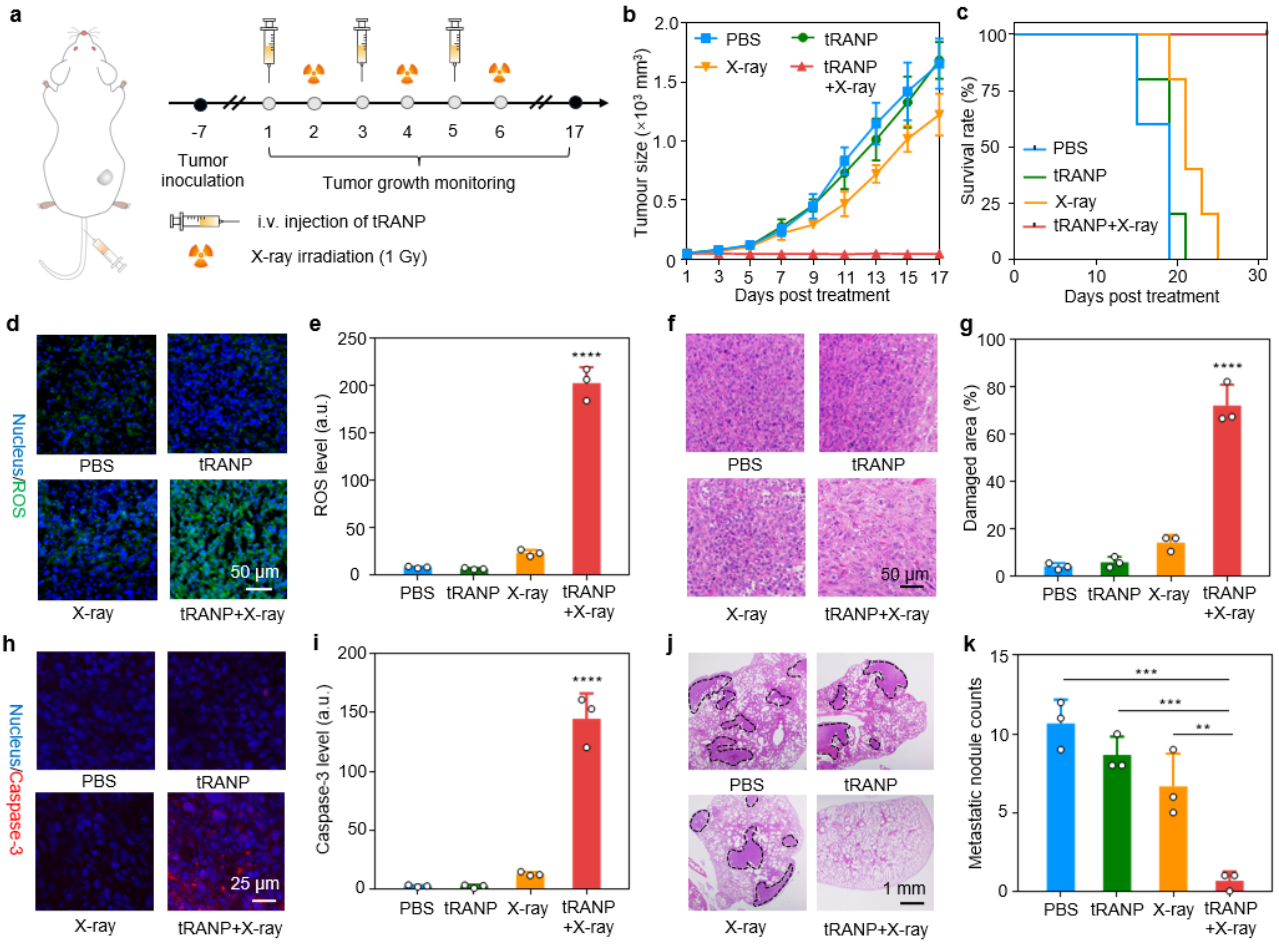

Fig. 6 | In vivo radiodynamic cancer therapy. (a) Timeline for tRANP-mediated radiodynamic therapy. Mice were intravenously injected with 100 μL of tRANP ([NIR775] = 100 μg/mL) on day 1, 3, and 5, followed by each fraction of X-ray (1 Gy) on tumours on day 2, 4, and 6. **(b)** Tumour growth curve of mice after indicated treatments (n = 5 mice). **(c)** Survival rate of mice after indicated treatments (n = 5 mice). **(d)** Representative confocal images of intratumoral ROS measured by SOSG from mice after indicated treatments. **(e)** Quantification of intratumoral ROS signals in (d). n = 3 independent samples. ****p < 0.0001 versus PBS (1.6×10^{-8}), X-ray (3.0×10^{-8}) and tRANP (1.5×10^{-8}). **(f)** Representative images of H&E-stained tumour sections from mice after indicated treatments. **(g)** Quantification of damaged area in (f). n = 3 independent samples. ****p < 0.0001 versus PBS (6.6×10^{-7}), X-ray (2×10^{-6}) and tRANP (8.1×10^{-7}). **(h)** Representative images of anti-caspase-3 antibody-stained tumour sections from mice after indicated treatments. **(i)** Quantification of caspase-3 signals in (h). n = 3 independent samples. ****p < 0.0001 versus PBS (1×10^{-6}), X-ray (2×10^{-6}) and tRANP (1×10^{-6}). **(j)** Representative images of H&E-stained lungs sections of mice after indicated treatments. Dashed circles showed the metastatic nodules. **(k)** Counts of pulmonary metastatic nodules in mice after indicated treatments. n = 3 independent samples. *** p = 0.000132 (versus PBS), *** p = 0.000635 (versus tRANP), ** p = 0.004140. Data were presented as mean ± s.d. Statistical significance was calculated via one-way ANOVA followed by Tukey's post hoc test (e,

g, i and k).

References

1 Gao, X., Cui, Y., Levenson, R. M., Chung, L. W. & Nie, S. In vivo cancer targeting and imaging with semiconductor quantum dots. *Nat Biotechnol* **22**, 969-976 (2004).

2 Hong, G., Antaris, A. L. & Dai, H. Near-infrared fluorophores for biomedical imaging. *Nat Biomed Eng* **1**, 0010 (2017).

3 Waterhouse, D. J., Fitzpatrick, C. R. M., Pogue, B. W., O'Connor, J. P. B. & Bohndiek, S. E. A roadmap for the clinical implementation of optical-imaging biomarkers. *Nat Biomed Eng* **3**, 339-353 (2019).

4 So, M. K., Xu, C., Loening, A. M., Gambhir, S. S. & Rao, J. Self-illuminating quantum dot conjugates for in vivo imaging. *Nat Biotechnol* **24**, 339-343 (2006).

5 Jiang, Y. & Pu, K. Molecular Probes for Autofluorescence-Free Optical Imaging. *Chem Rev* **121**, 13086-13131 (2021).

6 Miao, Q. *et al.* Molecular afterglow imaging with bright, biodegradable polymer nanoparticles. *Nat Biotechnol* **35**, 1102-1110 (2017).

7 le Masne de Chermont, Q. *et al.* Nanoprobes with near-infrared persistent luminescence for in vivo imaging. *Proc Natl Acad Sci U S A* **104**, 9266-9271 (2007).

8 Jiang, Y. *et al.* A generic approach towards afterglow luminescent nanoparticles for ultrasensitive in vivo imaging. *Nat Commun* **10**, 2064 (2019).

9 Wu, L. *et al.* H(2)S-activatable near-infrared afterglow luminescent probes for sensitive molecular imaging in vivo. *Nat Commun* **11**, 446 (2020).

10 Qu, R. *et al.* Afterglow/Photothermal Bifunctional Polymeric Nanoparticles for Precise Postbreast-Conserving Surgery Adjuvant Therapy and Early Recurrence Theranostic. *Nano Lett* **23**, 4216-4225 (2023).

11 Chen, W. *et al.* Near-Infrared Afterglow Luminescence of Chlorin Nanoparticles for Ultrasensitive In Vivo Imaging. *J Am Chem Soc* **144**, 6719-6726 (2022).

12 Ni, X. *et al.* Near-Infrared Afterglow Luminescent Aggregation-Induced Emission Dots with Ultrahigh Tumour-to-Liver Signal Ratio for Promoted Image-Guided Cancer Surgery. *Nano Lett* **19**, 318-330 (2019).

13 Wei, X. et al. Leveraging Long-Distance Singlet-Oxygen Transfer for Bienzyme-Locked Afterglow Imaging of Intratumoral Granule Enzymes. *J Am Chem Soc* **146**, 17393-17403 (2024).

14 Maldiney, T. *et al.* The in vivo activation of persistent nanophosphors for optical imaging of vascularization, tumours and grafted cells. *Nat Mater* **13**, 418-426 (2014).

15 Chen, H. *et al.* LiGa(5)O(8):Cr-based theranostic nanoparticles for imaging-guided X-ray induced photodynamic therapy of deep-seated tumours. *Mater Horiz* **4**, 1092-1101 (2017).

16 Pei, P. *et al.* X-ray-activated persistent luminescence nanomaterials for NIR-II imaging. *Nat Nanotechnol* **16**, 1011-1018 (2021).

17 Zhang, C. *et al.* Marriage of scintillator and semiconductor for synchronous radiotherapy and deep photodynamic therapy with diminished oxygen dependence. *Angew Chem Int Ed Engl* **54**, 1770-1774 (2015).

18 Li, J., Cheng, F., Huang, H., Li, L. & Zhu, J. J. Nanomaterial-based activatable imaging probes: from design to biological applications. *Chem Soc Rev* **44**, 7855-7880 (2015).

19 Wang, X. & Pu, K. Molecular substrates for the construction of afterglow imaging probes in disease diagnosis and treatment. *Chem Soc Rev* **52**, 4549-4566 (2023).

20 Huang, J. *et al.* Molecular radio afterglow probes for cancer radiodynamic theranostics. *Nat Mater* **22**, 1421-1429 (2023).

21 Huang, J. *et al.* Chemiluminescent Probes with Long-Lasting High Brightness for In Vivo Imaging of Neutrophils. *Angew Chem Int Ed Engl* **61**, e202203235 (2022).
22 Wei, X. *et al.* Highly Bright Near-Infrared Chemiluminescent Probes for Cancer Imaging and Laparotomy. *Angew Chem Int Ed Engl* **62**, e202213791 (2023).
23 Yang, Z. et al. Recent advances in organic thermally activated delayed fluorescence materials. *Chem Soc Rev* **46**, 915-1016 (2017).
24 Ma, W. *et al.* Thermally activated delayed fluorescence (TADF) organic molecules for efficient X-ray scintillation and imaging. *Nat Mater* **21**, 210-216 (2022).
25 Hong, X. et al. TADF molecules with π-extended acceptors for simplified high-efficiency blue and white organic light-emitting diodes. *Chem* **8**, 1705-1719 (2022).
26 Gorrini, C., Harris, I. S. & Mak, T. W. Modulation of oxidative stress as an anticancer strategy. *Nat Rev Drug Discov* **12**, 931-947 (2013).
27 Lippert, A. R., Van de Bittner, G. C. & Chang, C. J. Boronate oxidation as a bioorthogonal reaction approach for studying the chemistry of hydrogen peroxide in living systems. *Acc Chem Res.* **44**, 793-804 (2011).
28 Chen, Z. Z. *et al.* Low Dose of X-Ray-Excited Long-Lasting Luminescent Concave Nanocubes in Highly Passive Targeting Deep-Seated Hepatic Tumours. *Adv Mater* **31**, e1905087 (2019).
29 Lo, S. S. *et al.* Stereotactic body radiation therapy: a novel treatment modality. *Nat Rev Clin Oncol* **7**, 44-54 (2010).
30 Stupp, R. *et al.* Radiotherapy plus concomitant and adjuvant temozolomide for glioblastoma. *N Engl J Med* **352**, 987-996 (2005).
31 Hymes, S. R., Strom, E. A. & Fife, C. Radiation dermatitis: clinical presentation, pathophysiology, and treatment 2006. *J Am Acad Dermatol* **54**, 28-46 (2006).

Methods

Chemicals. All reagents were purchased from Sigma-Aldrich unless otherwise described. 4CzTPN-tBu (CzTPN) was ordered from Ossila (U.S.A). PBS, penicillin–streptomycin, high-glucose Dulbecco's modified Eagle's medium (DMEM) and fetal bovine serum (FBS) were obtained from Gibco. CCK-8 kit, Hoechst 33342, 4,6-diamidino-2-phenylindole (DAPI), Annexin-FITC, propidium iodide (PI) were ordered from Beyotime (China). DPAs was synthesized according to our previous reports.[21]

Composition screening. The candidate radioabsorbers, radiosensitizers, and radio-afterglow substrateswere dissolved in organic solvents to prepare the stock solution (1 mg/mL), respectively. Amphiphilic polymers (F127, DSPE-PEG, and PLGA-PEG) were dissolved in THF to prepare the stock solution (20 mg/mL), respectively. Amphiphilic polymer, radioabsorber, radiosensitizer, and radio-afterglow substrate were mixed at a mass ratio of 500: 10: 1: 2.5 in a flask, followed by evaporation of all organic solvents. The dried film was hydrated with aqueous solvent (such as deionized water or 0.01 M pH 7.4 PBS) under vigorous vortex, yielding transparent solution of nanoparticles. [Radioabsorber] = 100 μg/mL (PS, 2.5×10^{-3} μmol/mL; AT, 5.6×10^{-1} μmol/mL; 3.0×10^{-1} μmol/mL; CzTPN, 8.1×10^{-2} μmol/mL), [Radiosensitizer] = 10 μg/mL (HMP, 1.7×10^{-2} μmol/mL; VP, 1.4×10^{-2} μmol/mL; NIR775, 7.5×10^{-3} μmol/mL), [Radio-afterglow substrate] = 25 μg/mL (DPAs, 5.0×10^{-2} μmol/mL; DTDP, 5.4×10^{-2} μmol/mL). Specifically, RANP was developed by F127, CzTPN, NIR775, DTDP at a mass ratio of 500: 10: 1: 2.5 after optimization. [CzTPN] = 100 μg/mL (8.1×10^{-2} μmol/mL), [NIR775] = 10 μg/mL (7.5×10^{-3} μmol/mL), [DTDP] = 25 μg/mL (5.4×10^{-2} μmol/mL). The

excess F127 was removed via ultrafiltration (MWCO 3500) at 4,000 rpm for 10 min. The morphology of RANP was characterized using transmission electron microscope (TEM, JEOL JEM 1400), and hydrodynamic size and zeta potential were determined using Malvern Nano-ZS.

Optical properties characterization. CzTPN was dissolved in dichloromethane, NIR775 and DTDP (and caged DTDP) in tetrahydrofuran. Nanoparticles were dissolved into PBS (pH 7.4, 0.01 M). The absorbance spectra were recorded using GENESYS™ 50 UV-Vis spectrophotometers (Thermo Fisher, U.S.A.). The fluorescence spectra were recorded using F-4600 fluorescence spectrophotometer (Hitachi, Japan). X-ray was generated using a miniature, lab-standard, portable X-ray tube ordered from Moxtek. Inc. USA. Parameters: target material, tungsten; maximum tube voltage, 70 KV; maximum tube current, 1000 μA; PC I2C control). By adjusting the voltage, current, distance between sample and X-ray, the dose rate of X-ray can be adjusted from μGy/s to Gy/s applied on sample according to manufacturer's instruction. The dose rate under different conditions were calibrated using an X-ray dosimeter (Raysafe, R/F X2X, FLUKE). For radioluminescence measurement, the portable X-ray tube was equipped with fluorometer, by which the samples were irradiated with real-time X-ray while the emission was recorded using detector of fluorometer. Radioluminescence was also recorded by X-ray tube-incorporated in vivo imaging system (IVIS, Artemis Intelligent Imaging. Inc., China). For radio-afterglow measurement, the emission was recorded after cessation of X-ray irradiation by fluorometer. The radio-afterglow intensities were measured using luminometer (Promega, Glomax^{TM}) and IVIS. X-ray responsiveness was tested by radioafterglw measurement under different X-ray dosages (0.1-2.0 Gy). Limit of detection (LOD) was calculated by 3 σ/s, where σ denotes the standard deviation of blank samples and s denotes the slope of calibration curve.

Synthesis of caged DTDP (cDTDP). Compound 1 (936 mg, 4 mmol) and 3 mL of anhydrous THF were added into a round bottom flask (RBF) with a stirring bar (**Scheme S1**). The system was relocated into an ice bath and left to stir for 10 min. Phosphorus tribromide (PBr_3) (2160 mg, 8 mmol) was dissolved with 2 mL of anhydrous THF and then injected into the reaction system over 5 min. The reaction was left to react for 2 h, and the system was quenched with the addition of the DCM (50 mL) and then washed with concentrated Na_2CO_3 solution 2 times. The organic phases were collected and dried over Na_2SO_4, and then concentrated by the rotary evaporation. The liquid product was freeze-dried overnight and directly used for the next step without further purification. DPT was prepared according to previously reported method.[22] DT (46.6 mg, 0.1 mmol), compound 2 (118 mg, 0.4 mmol), potassium carbonate (K_2CO_3) (10 mg, 0.75 mmol), cesium carbonate (Cs_2CO_3) (24 mg, 0.75 mmol), and 3 mL of anhydrous acetonitrile were added into a round bottom flask with a stirring bar. The reaction was conducted under room temperature and the progression was monitored with TLC. Once there was no DT could be observed on the TLC plate, the reaction was stopped and purified by column chromatography with DCM/Methanol (100:1), affording DPDT as a yellow solid. Proton-nuclear magnetic resonance (^{1}H NMR) spectra were recorded on a Bruker Advance II 400 MHz NMR. 1H NMR (400 MHz, $CDCl_3$) δ 7.83 (d, *J* = 7.6 Hz, 2H), 8.09 (d, *J* = 8.4 Hz, 1H), 7.39 (d, *J* = 8.0 Hz, 2H), 7.35 (d, *J* = 11.2 Hz, 1H), 6.87 (s, 1H), 6.85 (d, *J* = 11.2 Hz, 1H), 6.79 (s,1H), 6.77 (d, *J* = 10.4 Hz, 1H), 5.21 (s, 2H), 3.33 (s, 1H), 3.29 (s, 3H), 2.60 (s, 2H), 2.43 (s, 2H), 2.08-1.72 (m, 12H), 1.07 (s, 6H). LC-MS analyses were tested with Triple Quadrupole LC/MS (Agilent 1260-6460). MS (ES+): m/z calc. for 682.39; found: 681.54 $[M - H]^{-1}$.

H_2O_2 responsiveness of cDTDP and tRANP. cDTDP ([DTDP] = 10 μM) was incubated with or without H_2O_2 (20 μM) in PBS (0.01 M, pH 7.4) for 10 min followed by analysis with HPLC. tRANP was incubated with or without H_2O_2 (20 μM) in PBS (0.01 M, pH 7.4) for 10 min, followed by X-ray irradiation (1 mGy). The radio-afterglow was recorded using fluorometer with excitation off and using IVIS (exposure time 10 s). RANP was also incubated with other ROS including superoxide anion ($O_2^{\cdot-}$), nitric oxide (NO), and hydroxyl radicals (·OH) at same concentration for comparison.

Deep-tissue penetration assay. RANP ([DTDP] = 100 μg/mL) in PBS (0.01 M, pH 7.4) was first irradiated with laser (680 nm, 0.3 W/cm^2) or X-ray (50kV, 200 μA) without any coverage to obtain the same afterglow signals. Afterwards, RANP solutions were put beneath chicken breast tissues of different thicknesses (2.5, 5, 10 ,15 cm) and irradiated with laser or X-ray, followed by the afterglow imaging after removing tissues using in vivo imaging system. In another set of studies, samples were irradiated, and afterglow signals were detected through chicken breast tissues of different thicknesses (1.5, 3.5, 5 cm). Exposure time was set at 30 s.

Radio-afterglow induction on cells. 4T1 cancer cells (or MCF-7 cancer cells) were seeded onto glass-bottom dishes (2×10^5 per dish) and incubated in complete DMEM (containing 10% FBS and 1% penicillin-streptomycin) for 24 h. Cells were then incubated with or without RANP ([DTDP] = 20 μg/mL) for 12 h, followed by X-ray irradiation (1 mGy) or not. Radio-afterglow signals were immediately captured using inverted microscope (Leica, German) with open filter and any excitation off. Exposure time was set at 10 s. For the observation of cells treated with tRANP, the media was added with H_2O_2 (20 μM) and incubated for 0.5 h before tRANP incubation. In another set of experiment, MCF-7 cells in glass-bottom dishes (2×10^5 per dish) were incubated with CzTPN nanoparticles ([CzTPN] = 80 μg/mL), NIR775 nanoparticles ([NIR775] = 8 μg/mL), DTDP nanoparticles ([DTDP] = 20 μg/mL) for 12 h, irradiated with X-ray irradiation (1 mGy), and immediately imaged under inverted microscope with any excitation off. In the third set of experiment, MCF-7 cells in glass-bottom dishes (2×10^5 per dish) were pre-incubated with tryptophan (5 mM) for 6 h and incubated with RANP ([DTDP] = 20 μg/mL) for 12 h, followed by X-ray irradiation (1 mGy) and imaging under inverted microscope.

In vitro ROS detection. For $^1O_2$ measurement, RANP in PBS ([CzTPN] = 100 μg/mL, [NIR775] = 10 μg/mL) was supplemented with 4-amino-2,2,6, 6-tetramethylpiperidine (TEMP, 10 mM), followed by X-ray irradiation (1 Gy). The samples were immediately detected using ESR. For superoxide anion and hydroxyl radical detection, RANP in PBS ([NIR775] = 10 μg/mL) was supplemented with 5,5-dimethyl-1-pyrroline N-oxide (DMPO, 100 mM). Samples after radiation were immediately analyzed using electron spin resonance (ESR). RANP in PBS ([NIR775] = 40 μg/mL) was also put beneath chicken breast tissues of different thicknesses prior to X-ray irradiation and $^1O_2$ was determined using ESR.

Cell viability assay. 4T1 cancer cells (or MCF-7 cancer cells) were seeded onto 96-well plate (2×10^4 per well) and incubated for 24 h. Cells were incubated with or without RANP ([NIR775] = 5, 10, 20, 40, 80 μg/mL) for 12 h and irradiated with or without X-ray (0.5 Gy), followed by further incubation for 12 h. Cells without any treatment was set as control. Cells were then incubated with CCK-8 agent (10 μL per well) for 2 h, and the absorbance of each well was determined at 450 nm using microplate reader (BioTek, Lonza, Switzerland). The cell viability was calculated as (mean OD_{sample} – Mean

OD_{blank})/ (mean $OD_{control}$ – Mean OD_{blank}) × 100%. In another set, 4T1 cancer cells were treated with RANP at a fixed concentration of [NIR775] = 20 μg/mL for 12 h, and irradiated with different doses of X-ray (0.2, 0.5, 1, 1.5, 2.0 Gy). To mimic cell killing in deep tissues, cells were treated with RANP ([NIR775] = 20 μg/mL) and irradiated with X-ray (0.5 Gy) through chicken tissue of different thicknesses (5, 10, 15, 20 cm). Cells without any treatment was set as control group.

Cell apoptosis study. 4T1 cells (or MCF-7 cells) were seeded onto 6-well plate and incubated for 24 h. The media were refreshed and supplemented with or without RANP ([NIR775] = 20 μg/mL) and incubated for 12 h. Afterwards, cells were irradiated with X-ray (0.5 Gy) and incubated for another 12 h. Cells were stained with Annexin V-FITC (1:100) and PI (1:100) for 20 min in dark according to manufacturer's instructions. The stained cells were analyzed using flow cytometry (CytoFLEX, Beckman Coulter, U.S.A.).

Intracellular ROS detection. 4T1 cancer cells (or MCF-7 cancer cells) were seeded onto glass-bottom dishes (2×10^5 per dish) and incubated for 24 h. Cells were incubated with or without RANP ([NIR775] = 20 μg/mL) for 12 h, followed by incubation with dichloro-dihydro-fluorescein diacetate (DCFH-DA) for another 2 h. Cells were then irradiated with X-ray (0.5 Gy) or not. Cells were stained with Hoechst 33342 (1: 200), followed by fluorescence observation under confocal laser scanning microscope (CLSM, Leica, German).

Animal models. All animal experiments were conducted in accordance with the guidelines approved by Ethics Committee of China-Japan Friendship Hospital (China) and Guidelines for Care and Use of Laboratory Animals of the NTU Institutional Animal Care and Use Committee (IACUC, Singapore). For all animal experiments, Balb/c mice (5-6 wks, female) were ordered from GemPharmatech Inc. (China). Mice were kept in ventilated clear plastic cages under appropriate ambient temperature (~22 °C), humidity (50%) and standard 12 h: 12 h light: dark conditions. The subcutaneous tumour model was established by subcutaneous injection of 100 μL of 4T1 cancer cells (2×10^6) into the right flank of mice. Abdominal metastatic model was established by intraperitoneally injecting with 100 μL of 4T1 cancer cells (2×10^6). At 7 days post inoculation, mice were randomly divided into different groups for indicated treatments. X-ray was irradiated solely on tumours (or subcutaneously injected sites) with other parts of body covered with lead shield. Mice were anesthetized with isoflurane/oxygen system during in vivo imaging and surgery. After surgery, mice were additionally treated with meloxicam (2 mg/kg, p.o.) for a week for analgesia. Mice were euthanized when tumour size reaches 2000 mm^3 (under ethical approval).

In vivo radio-afterglow imaging. Subcutaneous 4T1 tumour-bearing mice (n = 3) were shaved to expose both left and right flank (with tumours). 10 μL of tRANP ([cDTDP] = 100 μg/mL) was subcutaneously injected to the left flank and intratumorally injected to the right flank. After 10 min, the two injection sites were irradiated with X-ray (1 mGy) and the afterglow signals were recorded using IVIS with open filter (acquisition time: 30 s). Fluorescence signals were recorded using IVIS equipped with 750 long-pass filter (excitation wavelength: 660 nm, acquisition time: 0.1 s). In another set of imaging study, subcutaneous 4T1 tumour-bearing mice (n = 3) were intravenously injected with 100 μL of tRANP ([cDTDP] = 250 μg/mL) and imaged at indicated time points (0, 3, 6, 12, 24, 36, 48 h) using IVIS under fluorescence and radio-afterglow modes. For radio-afterglow induction, X-ray (1 mGy) was irradiated on tumours at each time point. Acquisition time: 30 s.

Imaging-guided laparotomy. Abdominal 4T1 tumour-bearing mice (n = 3) were intravenously injected with 100 μL of tRANP ([cDTDP] = 250 μg/mL). After 12 h, the abdomen region was irradiated with X-ray (1 mGy), followed by radio-afterglow acquisition using IVIS. Exposure time: 30 s. Afterwards, mice were subjected to laparotomy by open the abdomen, followed by radio-afterglow acquisition using IVIS without further X-ray irradiation. Tumours were carefully collected under the guidance of radio-afterglow imaging and subjected to histological analysis (see below), and mice were subjected to surgical suture and monitored after surgery. Fluorescence signals were recorded using IVIS (excitation wavelength: 660 nm, acquisition time: 0.1 s).

tRANP-mediated radiotherapy in vivo. On day 1, 4T1 tumour-bearing mice (n = 5 for each group) were divided to four groups and treated with PBS, X-ray only, tRANP only, or tRANP plus X-ray. 100 μL of tRANP ([NIR775] = 100 μg/mL) was intravenously injected with and X-ray (1 Gy) was irradiated on tumours after 24 h. The indicated treatments were conducted on day 3 and 5 as well. The X-ray dosages were optimized with 4T1 tumour-bearing mice (n = 3 for each group) under 3 fractions of 0.5, 1 and 2 Gy, respectively. For comparison, tRANP-free 4T1 tumour-bearing mice (n = 3) were subjected to X-ray (6 Gy × 3 fractions), which mimic clinical radiotherapy. Tumours were measured every two days and volumes were calculated via the formula: $V = 1/2\ ab^2$, where a is the length and b is the width of tumour mass. Tumour inhibition rate was calculated by (1 – (mean volume of treated tumours)/(mean volume of PBS-treated tumours)) × 100%. Survival analysis was conducted with Kaplan-Meier estimate using GraphPad Prism 7.0.4.

Intratumoral ROS detection. 4T1 tumour-bearing mice were intravenously injected with 100 μL of tRANP ([NIR775] = 100 μg/mL). At 12 h post injection, singlet oxygen sensor green (SOSG, Thermo Fisher, 1:100) was intratumorally injected into tumours. After 15 min, tumours were irradiated with X-ray (1 Gy), and immediately collected from mice after sacrifice. Fresh tumours were subjected to frozen section and slices were counter-stained with DAPI (1: 200, Beyotime). The tissues slices were observed under confocal microscope.

Histological analysis. Main organs including heart, liver, spleen, lung, kidneys, and skin were collected for fixation with 4% PFA for 12 h, 30% sucrose for 24 h, and sectioned for hematoxylin and eosin (H&E) staining. The suspected tumours from laparotomy were also sectioned for H&E staining. Pulmonary metastatic nodules were counted prior to fixation and tissue staining. The sections were observed under an inverted microscope. For immunogenic cell death analysis, tumour sections we further stained with antibody against calreticulin (PA3-900, 1:200, Thermo Fisher Scientific) or high mobility group box 1 (HMGB-1, 3E3, Alexa Fluor 488-labelled, 1:200, Biolegend), as well as DAPI (1: 200). The immunofluorescent sections were observed under CLSM.

Safety profile. The body weights of mice were measured every two days until the end of experiments. Whole blood samples and sera were collected for the measurement of regular blood parameters and biochemical indicators, respectively, using an automatic analyzer (DRI-CHEM NX700V, Fujifilm, Japan). Blood samples were extracted from healthy mice and tumour-bearing mice treated with RANP. Sera were collected via centrifugation at 1000 rpm for 4 min and determined with commercial kits (Sigma Aldrich, U.S.A.) for blood urine nitrogen (BUN), creatinine, alanine transaminase (ALT) and Aspartate aminotransferase (AST) respectively, according to manufacturers' instruction.

Statistical analysis. All numeric data are presented as mean ± s.d. unless otherwise indicated. The significance between two groups was analyzed by two-tailed Student's t-test. The significance between multiple groups was analyzed by one-way analysis of variance (ANOVA) with Tukey's post hoc test. Statistical analysis was performed using Graphpad Prism 7.0.4. P values less than 0.05 were considered significant. *$p < 0.05$, **$p < 0.01$, ***$p < 0.001$, ****$p < 0.0001$.

Data Availability Statement

All relevant data supporting the findings of this study are available within the Article and its Supplementary Information, or from the corresponding authors on reasonable request. Source data are provided with this paper.